Calibration of optical tweezers with positional detection in the back-focal-plane

Simon F. Tolić-Nørrelykke[†] (corresponding author)
Max Planck Institute for the Physics of Complex Systems,
Nöthnitzer Strasse 38, 01187 Dresden, Germany
and
European Laboratory for Non-linear Spectroscopy,
via Nello Carrara 1, 50019 Sesto Fiorentino (Fl), Italy

Erik Schäffer[†] and Jonathon Howard
Max Planck Institute of Molecular Cell Biology and Genetics,
Pfotenhauerstrasse 108, 01307 Dresden, Germany

Francesco S. Pavone
European Laboratory for Non-linear Spectroscopy,
via Nello Carrara 1, 50019 Sesto Fiorentino (Fl), Italy

Frank Jülicher
Max Planck Institute for the Physics of Complex Systems,
Nöthnitzer Strasse 38, 01187 Dresden, Germany

Henrik Flyvbjerg
Isaac Newton Institute for Mathematical Sciences, Cambridge, U.K.
and
Biosystems Department and Danish Polymer Centre,
Risø National Laboratory, DK-4000 Roskilde, Denmark
(Dated: February 13, 2006)

We explain and demonstrate a new method of force- and position-calibration for optical tweezers with back-focal-plane photo detection. The method requires only a low level of instrumentation and can be applied *in situ* in all spatial dimensions. Since it does not use the drag coefficient of the trapped object as input, neither the viscosity, the size of the trapped object, nor its distance to nearby surfaces need to be known. The method is both accurate and precise: true values are returned, with small error-bars. We tested this experimentally, near and far from surfaces. Both position- and force-calibration were accurate to within 3%. To calibrate, we moved the sample with a piezo-electric translation stage, but the laser beam could be moved instead, e.g. by acousto-optic deflectors.

I. INTRODUCTION

Optical tweezers are dexterous instruments for grabbing and holding micron-sized objects in liquids. Optical tweezers can also be used to measure and exert forces. In order to use optical tweezers as a quantitative instrument for position and force measurements, the detection system must be calibrated. The position is calibrated by comparing the detector response to a known displacement. Likewise, the force on a trapped object is calibrated by exerting a known force on it. The two calibrations are closely related, since a trapped object experiences a Hookean force, $F = \kappa x$, for small displacements, x, from the trap's center. Thus, if the trap stiffness κ is known, a known displacement produces a known force, and a known force produces a known displacement. Two known forces are often used for position-calibration via this relationship: The thermal force causing Brownian motion, and the drag force exerted by a constant flow of known velocity.

Position detection schemes can be grouped into *imaging* and *non-imaging* [1, and references therein]. For imaging techniques, a known displacement is directly visualized. Calibration is performed by moving either the position of the detector or the trap in a controlled manner. In the case of non-imaging techniques, if trapping and tracking is done with the same laser, this approach does not work. A translation of the trap in the imaging plane does not give rise to a signal on the detector in this case. Only the position of the trapped object relative to the trap center is detected. In such a system, and these are the systems we are interested in here, the calibration

---

[†]These authors contributed equally to this work

is limited by how accurately the trapped object can be displaced relative to the laser by a *known* amount.

One method that creates such a relative displacement consists of moving a micro-sphere ("bead") fixed to the surface through the laser beam while recording the response of the detector. Although this movement is known with high accuracy, the method has several drawbacks: The bead used for the calibration cannot be used for further experiments (it is immobilized on the surface). Also, the calibration is done at zero bead-to-surface separation, which is not necessarily where the actual experiment or force calibration will take place. Finally, the exact location of the bead relative to the trapping position is not known. Two different lasers can be used for trapping and detection to circumvent these problems [2]. This approach is powerful, but technically demanding, as it requires a moveable trap and careful alignment of the two lasers.

For the reasons enumerated in the previous paragraph, the preferred calibration methods are those that can be done *in situ*, meaning on an individual bead located where the experiment is to be done. For *in situ* calibration, the power-spectrum method is widely used: The power spectrum of the trapped bead's thermally driven motion is fitted with a Lorentzian (or a more complicated expression), which returns an amplitude and a characteristic frequency with high precision [3]. From these, the trap stiffness and position calibration factor can be calculated, provided that the drag coefficient is known. This method, and all drag-force methods, suffer from the same problem, however: The drag coefficient is very sensitive to the viscosity of the surrounding liquid, the proximity of nearby surfaces, and the radius of the bead. So often the drag coefficient is not known precisely.

All in all, calibration of optical tweezers typically involves three unknowns: The volt-to-meter calibration factor β, the trap stiffness κ, and the drag coefficient γ. At most two of these unknowns are determined by any single method, so calibration is an under-determined problem. To solve this problem, either one must make assumptions about one of the unknowns, or an additional parameter must be measured in an independent manner. Usually, the drag coefficient is calculated using Stokes' formula $\gamma_{\text{Stokes}} = 6\pi\eta R$, with significant corrections when working close to surfaces [4]. The radius of the bead R, the dynamic viscosity η of the liquid, and the distance to nearby surfaces, all must be estimated. Because the drag coefficient and the trap stiffness both depend on the bead-to-surface distance, calibration should be done where the experiment will be performed. Even far from surfaces, the poly-dispersity of commercially available micro-spheres and the strong temperature dependence of the viscosity ($\approx 2\%$ per $^\circ$C) introduce errors. Furthermore, one has to rely on the specifications given by the manufacturer about the mean diameter of the micro-spheres. In a notable exception, the net optical force acting on a trapped bead was calculated from the total momentum transfer, found by collecting the light

scattered by the bead [5]. However, all scattered light must be collected, making it impractical for most single-beam laser tweezers.

In the present paper we present a method that allows calibration of the position- and force-detection system for individual micro-spheres at the position where the experiment is performed. It combines the precision of power spectral analysis for optical tweezers [3] with the accurate position control of an optical trap relative to the liquid environment. In the case of force calibration, the temperature enters only on the absolute scale, suppressing the influence of errors from temperature measurements ($\approx 0.3\%$ per $^\circ$C, at room temperature).

While we were adding the final touch to the present paper, another paper appeared that calibrates the position-detection system with a method that is different, but related in spirit [6]. We compare it to our method in the Discussion section below.

II.   MATERIALS AND METHODS

Measurements were done with two separate optical tweezers systems. Both use the trapping laser for non-imaging position detection in the back focal plane. One system has a long working distance and was used to test the method far from surfaces ($30\,\mu$m): This experimental setup is described in detail in [7] and briefly here. The instrument is based on a custom built inverted microscope with a Nikon, $60\times$, 1.2 NA, 0.2 mm working distance, Plan-Apo, water immersion objective. The laser is a 1064 nm, Nd:YAG (Spectra-Physics, Millennia IR). Position detection is done with a position sensitive photodiode (UDT DLS-20). Flow-cells with a volume of $10\,\mu l$ (dimensions $8\times20\times0.06\,\text{mm}^3$) were assembled by placing one coverslip No. 0 on top of a microscope slide separated by spacers of double-sticking tape. A dilute solution of beads was flowed in, and the ends were sealed with nail polish to avoid sample evaporation. The flow-cell was mounted upside down on a Physik Instrumente piezo-electric translation stage (P-527.2 C1).

The other system has a short working distance and was used to test the method close to surfaces (0–$3\,\mu$m): This experimental setup is described in detail in [8]. Briefly, it consists of a modified Zeiss Axiovert 135 TV microscope equipped with a Zeiss, $100\times$, 1.3 NA, Plan-Neofluar, oil-immersion objective. The laser is a 1064 nm, Nd:YVO$_4$ (Smart Laser Systems GmbH, Berlin, Germany). Position detection is obtained with a standard quadrant photodiode, QP50-6SD (Pacific Silicon Sensors Inc). Flow-cells with a 3 mm wide channel were assembled by placing one $18\,\text{mm}^2$ cover-slip No. 1.5 on top of a $22\,\text{mm}^2$ cover-slip No. 1.5 separated by a layer of parafilm. The parafilm was melted by placing the sample on a 100°C hot-plate. Cooling then glued the cover-slips together. A dilute solution of microspheres was flowed in, and the ends were sealed with vacuum grease to avoid sample evaporation. The flow-cell was mounted on a Physik In-

strumente piezoelectric translation stage (P-733.2 CL). For measurements close to the surface, the cover-slips were treated as described in [8] to reduce the influence of surface potentials.

The following beads were used: Silica beads from Bangs Laboratories (9025 Technology Drive, Fishers, IN 46038-2886, USA), catalog code SS04N, lot number 5303, were $1.54\,\mu m$ in diameter with a standard deviation of 10% (Coulter principle). Polystyrene microspheres from Polysciences (Warrington, PA 18976, USA), catalogue number 07307, lot number 50602, were $528\,nm$ in diameter with a 2% coefficient of variation. Transmission electron microscopy (TEM) of the latter microspheres indicated a standard deviation of 1.2%. The beads shrunk during the TEM observation, but the shape of the size distribution did not change (data not shown). Thus its relative standard deviation could be measured.

III. THEORY

In the following we discuss the theory for a calibration procedure in which the flow-cell is moved a known distance relative to the trapping laser by a piezo-electric translation stage. If, instead, the trap is moved a known distance relative to the flow-cell, the same formulae apply, provided the detector is placed in the back focal plane of the condenser. For clarity of presentation we omit frequency dependent corrections to the hydrodynamics. However, the full hydrodynamic theory [3] was used in the data analysis and is easily implemented.

A. Equation of motion

A microsphere suspended in water is trapped with optical tweezers inside a flow-cell. The stage moves the flow-cell sinusoidally relative to the optical trap with a frequency f_{drive} and an amplitude A, see Fig. 1, while the trap remains at rest in the laboratory system. The position of the stage x_{drive} as a function of time t is

$$x_{\mathrm{drive}}(t) = A\sin(2\pi f_{\mathrm{drive}}t) \ . \tag{1}$$

The stage velocity $v_{\mathrm{drive}}(t) \equiv \dot{x}_{\mathrm{drive}}(t)$ also corresponds to the velocity of the water in the flow-cell far away from the bead, since the water is at rest relative to the flow-cell (see Appendix A). After dropping all inertial terms, the equation of motion for a spherical bead in the trap is

$$\gamma\left[\dot{x}(t) - v_{\mathrm{drive}}(t)\right] + \kappa x(t) = F_T(t) \tag{2}$$

where $x(t)$ is the position of the bead relative to the center of the trap, γ is the drag coefficient, and κ is the trap stiffness. The first term on the left-hand-side is the drag force, which is proportional to the velocity of the bead relative to that of the stage. The second term on the left-hand-side is the trapping force. The right-hand

side is the random thermal force driving the Brownian motion. It has the properties

$$F_T(t) = \sqrt{2\gamma k_{\mathrm{B}}T}\,\xi(t) = \gamma\sqrt{2D}\,\xi(t) \tag{3}$$

with

$$\langle\xi(t)\rangle = 0\,; \ \ \langle\xi(t)\xi(t')\rangle = \delta(t-t') \tag{4}$$

where $k_{\mathrm{B}}T$ is the Boltzmann energy at absolute temperature T, the diffusion coefficient $D = k_{\mathrm{B}}T/\gamma$, ξ is a normalized white noise, and δ is Dirac's delta function.

B. Solution to the equation of motion

Since the equation of motion (2) is linear with two force terms, $\gamma v_{\mathrm{drive}}$ and F_T, its general solution can be written as a sum of two terms, one for each force,

$$x(t) = x_{\mathrm{response}}(t) + x_T(t) \ , \tag{5}$$

after transient initial behavior has died out. Here,

$$x_{\mathrm{response}}(t) = \frac{x_{\mathrm{drive}}(t - t_{\mathrm{lag}})}{\sqrt{1 + (f_c/f_{\mathrm{drive}})^2}} \ , \tag{6}$$

$$x_T(t) = \sqrt{2D}\int_{-\infty}^{t}\mathrm{d}t'e^{-2\pi f_c(t-t')}\,\xi(t') \tag{7}$$

where $t_{\mathrm{lag}} = [\arctan(f_{\mathrm{drive}}/f_c) - \pi/2]/(2\pi f_{\mathrm{drive}})$ and $f_c = \kappa/(2\pi\gamma)$. Figure 1b shows an example of an experimentally determined trajectory $x(t)$ of a bead in a trap, as described in Eq. (5). In this case, the stochastic thermal motion dominates and almost hides the driven, deterministic component of the motion.

In principle, we now could calibrate by fitting $x_{\mathrm{response}}(t)$ in Eq. (6) to data like those shown in Fig. 1b. However, this is not a reliable procedure [9]. Instead, we Fourier transform theory and data to the frequency domain where parameters are determined with optimal precision because the theory is simpler there.

C. Power spectrum

From Eqs. (5–7) it follows that the Fourier transform of $x(t)$ is

$$\begin{aligned}
\hat{x}(f) &= \int_{-\infty}^{\infty}\mathrm{d}t\,e^{i2\pi ft}x(t) \\
&= \frac{\hat{\xi}(f)\sqrt{2D}}{2\pi(f_c - if)} \\
&+ \frac{Ae^{i2\pi ft_{\mathrm{lag}}}}{2i\sqrt{1 + (f_c/f_{\mathrm{drive}})^2}}\left[\delta(f + f_{\mathrm{drive}}) - \delta(f - f_{\mathrm{drive}})\right] \ .
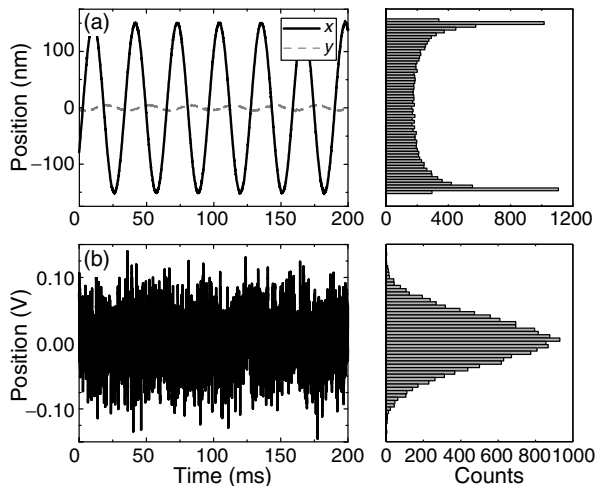\end{aligned} \tag{8}$$

FIG. 1: Position of the piezo-stage (a) and the trapped bead (b) when moving the stage sinusoidally with frequency $f_{\rm drive} = 32\,{\rm Hz}$ and amplitude $A = 150\,{\rm nm}$ in the x-direction. (a): Left, time series of stage position. Right, histogram of the x-data. The sinusoidal movement results in two clear maxima. (b): Left, time series of the bead's x-positions in volts, as given by the signal from the photodiode. The amplitude of the sinusoidal response is much smaller than the amplitude of the thermal motion. Consequently the sinusoidal shape is masked by the Brownian motion of the bead, and completely disappears in the histogram of visited positions.

Consequently, the expectation value for the one-sided ($f \geq 0$) power spectral density (PSD) of the bead positions is

$$
\begin{aligned}
P(f) \;=\; & \frac{2\langle|\hat{x}(f)|^2\rangle}{t_{\rm msr}} = P_T(f) + P_{\rm response}(f) \\
& \xrightarrow[t_{\rm msr}\to\infty]{} \frac{D}{\pi^2(f^2+f_c^2)} + \frac{\frac{1}{2}f_{\rm drive}^2 A^2}{f^2+f_c^2}\,\delta(f-f_{\rm drive})
\end{aligned}
\tag{9}
$$

where $t_{\rm msr}$ is the measurement time and $\langle\cdot\rangle$ denotes an average with respect to the thermal noise $\hat{\xi}$. This PSD consists of the familiar Lorentzian (first term, P_T), *plus* a delta-function spike (second term, $P_{\rm response}$) at the frequency with which the stage is driven. The Lorentzian comes from the Brownian motion of a bead in a parabolic potential and is hereafter referred to as the "thermal background". The power in this spike is known a priori in (meters)^2, hence is a "scale-bar" in the experimental power spectrum measured in (volts)^2. Specifically, Eq. (9) contains *three* parameters for us to determine from an experimental power spectrum: f_c, D, and A. This is one more parameter, A, than one has in a fit to the power spectrum of Brownian motion alone. Thus, the number of fitted parameters now equals the number of unknowns, and calibration is done without assumptions about γ.
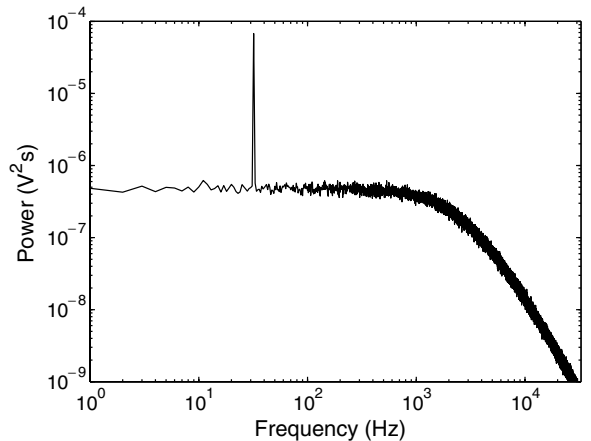

FIG. 2: Power spectrum of a $528\,{\rm nm}$ diameter polystyrene bead held in the laser trap with a corner-frequency $f_c = 2065 \pm 5\,{\rm Hz}$. The sample moves sinusoidally with amplitude $A = 150\,{\rm nm}$ and frequency $f_{\rm drive} = 32\,{\rm Hz}$. The power spectrum shown is the average of 100 independent power spectra. It consists of a thermal background caused by Brownian motion, plus a spike at $f_{\rm drive}$. The sampling frequency was $f_{\rm sample} = 65\,536\,{\rm Hz}$, the measurement time for each spectrum $t_{\rm msr} = 1\,{\rm s}$, and the temperature 24.4° C. For clear illustration, the measurement time used here is eight times longer than the one we typically use for calibration.

D. Positional calibration

The power in the peak in (meters)^2 follows from Eq. (9),

$$
W_{\rm th} = \int_0^{f_{\rm Nyq}} P_{\rm response}(f)\,{\rm d}f = \frac{\frac{1}{2}A^2}{1+(f_c/f_{\rm drive})^2} \ . \tag{10}
$$

Thus, the desired calibration factor for distances is

$$
\beta = \sqrt{W_{\rm th}/W_{\rm ex}}\,, \quad [\beta] = {\rm m/V} \ , \tag{11}
$$

where $W_{\rm ex}$ is the experimentally determined power in the peak, measured in (volts)^2.

E. Force calibration

The trap's force on a bead is κx. With the position detection system calibrated, the displacement x is measured in meters. To determine the trap stiffness κ, we use that $\kappa = 2\pi k_{\rm B} T f_c/D$ where f_c and D are determined by fitting the first term in Eq. (9) to the thermal background in the experimental PSD. The local temperature T of the liquid can typically be determined with sufficient accuracy by direct measurement in or near the flow-cell: T is the absolute temperature, so an absolute error of $1\,{\rm K}$ results in a relative error of only 0.3%.

IV. HOW TO CALIBRATE

Three steps are necessary for calibration: (1) Determination of the total power in the spike; (2) Fitting of the thermal background; (3) Subtraction of the thermal background from the total power in the spike.

1. Power in the spike

The power in the spike, in $(\text{volts})^2$s, can be determined from the PSD: In an experiment, the measurement time t_{msr} is fixed, so the spike (scale-bar) is no longer a delta-function. The height of the spike is now finite, and directly proportional to t_{msr}. Its width is also finite in general, due to *leakage* [10] [11, Fig. 5]. However, if calibration data are taken for a time t_{msr} that is an *integer multiple* of the period of the stage movement, then f_{drive} is an integer multiple of the frequency resolution $\Delta f = 1/t_{\text{msr}}$, and the spike consequently consists of a single datum [10].

Obviously, t_{msr} can also be *trimmed* to an integer multiple of the period of the stage *after* calibration data have been taken. However, fast Fourier transformation requires the number of points in a time series to be a power of 2. So trimming may mean discarding up to half of ones data.

2. Fitting the PSD away from the spike

Depending on the precision desired, two approaches are possible. If precision is not a major concern, the PSD away from the spike can be fitted with a Lorentzian [12], i.e., with the expression given by P_T in Eq. (9). When precision is required, a more complete theory must be used. This theory should include the frequency dependence of the drag coefficient, treat the photo-diode as a low-pass filter, account for aliasing, and model the electronic filters used during the data acquisition [3]. Both methods will return two fit parameters, the corner frequency, f_{c}, in Hz and the diffusion coefficient, D_{V}, in $(\text{volts})^2/\text{s}$.

3. Subtracting the thermal background

If the spike is several orders of magnitude above the thermal background, as in Fig. 2, the thermal background can be ignored. If not, the thermal background must be subtracted from the total power in the spike to find the contribution from the forced motion, given by P_{response} in Eq. (9). The value of the thermal background can be found by fitting the PSD away from the spike and then extrapolating this fit to the position of the spike.

Then, the power in the spike is

$$W_{\text{ex}} = \left(P_{\text{V}}(f_{\text{drive}}) - \frac{D_{\text{V}}}{\pi^2(f_{\text{drive}}^2 + f_{\text{c}}^2)} \right) \Delta f \qquad (12)$$

where $P_{\text{V}}(f_{\text{drive}})$ is the experimentally determined value of the PSD at f_{drive} measured in $(\text{volts})^2$s. The second term on the right-hand-side is the PSD of the thermal background at f_{drive}.

A. Determining the calibration factor

When the spike consists of a single datum, the power in the spike can be found by multiplying the value of the PSD at f_{drive} by Δf. In this case we have

$$\beta \simeq \frac{A f_{\text{drive}}}{f_{\text{c}} \sqrt{2 P_{\text{V}}(f_{\text{drive}}) \Delta f}} \quad . \qquad (13)$$

This approximation is better than 1%, provided $f_{\text{c}}/f_{\text{drive}} > 10$, and the spike is two or more orders of magnitude above the thermal background. When the last two conditions are not satisfied

$$\beta = \frac{A f_{\text{drive}}}{\sqrt{2 \left\{ P_{\text{V}}(f_{\text{drive}})[f_{\text{drive}}^2 + f_{\text{c}}^2] - D_{\text{V}}/\pi^2 \right\} \Delta f}} \quad . \qquad (14)$$

Once the calibration parameter has been determined for the trapped object, the experimentally determined drag coefficient

$$\gamma_{\text{ex}} = \frac{k_{\text{B}} T}{\beta^2 D_{\text{V}}} \qquad (15)$$

and trap stiffness

$$\kappa_{\text{ex}} = 2\pi f_{\text{c}} \gamma_{\text{ex}} \qquad (16)$$

can be calculated directly from the fit parameters f_{c} and D_{V}.

V. EXPERIMENTAL RESULTS

The key advantage of the calibration method presented here is that it does not depend on an assumed value for the bead's drag coefficient. On the contrary, that value results from the calibration by virtue of Einstein's relation

$$D = k_{\text{B}} T / \gamma \qquad (17)$$

if the temperature is known. In order to test the accuracy and advantage of our calibration method, we now compare our experimentally determined value for the drag coefficient with the value we would have been forced to assume, had we used another calibration method.

We determined the drag coefficient both far from and close to surfaces. Fitting of the PSD of the thermal background was done with as high a precision as possible using either published Matlab routines [13, 14] or custom

written software in LabView [8]. These fitting routines take into account hydrodynamics corrections, aliasing, parasitic filtering in the photo diode, and electronic filters in the data acquisition [3].

A. Measurements in bulk

First we measured the drag coefficient far from surfaces, where γ_{ex} can be compared directly to Stokes's formula. Beads were trapped near the bottom of the flow-chamber (silica beads are heavier than water) and brought to the middle of the flow-cell, $30\,\mu m$ from the bottom and the top, to minimize the effect of nearby surfaces. The x-axis—the direction of motion—was chosen perpendicular to the long axis of the flow-cell and to the direction of the incoming laser light. The experimental parameters were: $A = 208\,nm$, $f_{drive} = 28\,Hz$, $f_{sample} = 20\,kHz$, $t_{msr} = 13\,s$, $2R = 1.54\,\mu m$, $T = 23.0$ °C, and $f_c = 584 \pm 10$ (mean $\pm$ SE, $n = 21$).

Figure 3 illustrates the effect of choosing a value of f_{drive} that does not match t_{msr}: The spike at f_{drive} is broadened due to the leakage of power to neighboring frequencies. The figure also illustrates the effects of windowing: Leakage of power to neighboring frequencies is suppressed and the power in the peak is distributed to a few frequencies near f_{drive}. Thus, the power in the peak was found by summing the five data points closest to f_{drive} after subtraction of the thermal background. The conversion factor was found using Eq. (11) after calculation of W_{th} from Eq. (10).

The measured value for γ_{ex} was $(1.36 \pm 0.02) \times 10^{-8}\,kg/s$ (mean $\pm$ standard error (SE), $n = 21$), i.e., the measured drag coefficient showed a standard deviation of 5.4%, which agrees with the 10% variation in bead diameter listed by Bangs because of our limited sample size. The expected value for the drag coefficient is $\gamma_{Stokes} = (1.35 \pm 0.14) \times 10^{-8}\,kg/s$ (mean $\pm$ standard deviation (SD)) where the error is propagated from the combined uncertainty about the viscosity and the variation in bead diameter given by the producer. These results suggest that the method is both accurate and precise, even when choosing non-ideal parameters for driving and sampling.

B. Measurements near surfaces

In practice, experiments are often done close to a surface, such as a cover slip. Working close to a surface—in our case $< 3\,\mu m$—complicates standard calibration techniques especially if a high numerical aperture oil-immersion objective is used. Aberrations arising from a refractive index mismatch at the glass-water interface cause a linear decrease in stiffness away from the surface and a focal shift [15–17].
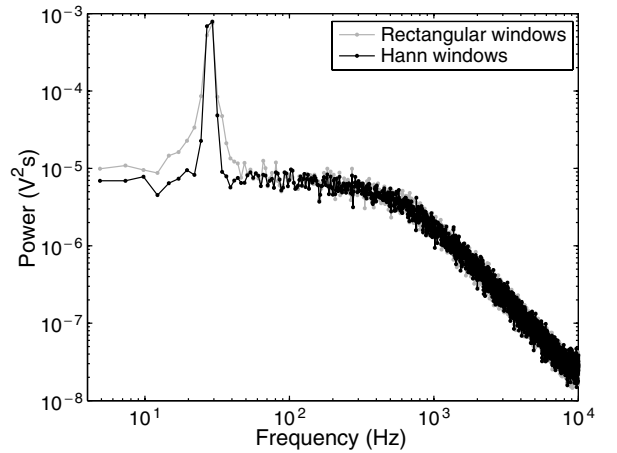

FIG. 3: Power spectrum of a $1.54\,\mu m$ diameter silica bead held in the laser trap with a corner-frequency $f_c = 600 \pm 13\,Hz$. The sample moves sinusoidally with amplitude $A = 208\,nm$ and frequency $f_{drive} = 28\,Hz$. The power spectrum shown is the average of 32 independent power spectra. It consists of a thermal background caused by Brownian motion, plus a spike at f_{drive}. The sampling frequency was $f_{sample} = 20\,kHz$, the measurement time for each spectrum $t_{msr} = 0.41\,s$, and the temperature 23.0 °C. The grey line shows the PSD when rectangular windows are used with a broadening of the spike at f_{drive} caused by the leakage of power to neighboring frequencies. The black line shows the PSD when Hann windows are used. The use of Hann windows suppresses leakage of power to neighboring frequencies.

1. Acquisition and fitting

The experimental parameters were: $A = 150\,nm$, $f_{drive} = 32\,Hz$, $f_{sample} = 65\,536\,Hz$, $t_{msr} = 1/8\,s$, $2R = 528\,\mu m$, and $T = 24.4$°C. Power spectra that resulted from averaging 100 experimental spectra were fitted with a custom-written least-squares fitting routine (Labview, NI). Each datum was weighted by its theoretical error bar [3]. The fit was done from $8\,Hz$ to $25\,kHz$ omitting the single datum at the stage frequency $f_{drive} = 32\,Hz$.

For every trapped bead the calibration factor, the drag coefficient, and the trap stiffness were found at each of 50 distances to the surface. The exact surface position was obtained from a fit of the drag coefficient to Faxén's law taking the focal shift into account. Thus, the quoted values for γ_{ex} are the measured values extrapolated to bulk, corresponding to γ_{Stokes}. More details for the above procedure can be found in [8].

2. Temperature

To compare our experimentally determined value for the drag coefficient with the theoretically expected value, we need to know the temperature of the liquid. We measured this temperature with a small thermocouple introduced into the flow cell, while simultaneously recording

the temperature of the imaging and condenser objective, and the room temperature. The temperatures of the two objectives differed by 0.5 °C. The temperature inside the flow cell was intermediate between these and was measured to within 0.2 °C. We estimated an upper limit of 0.5 °C for the temperature increase due to laser heating [18]. Thus, the propagated error on γ_{ex} from uncertainty about the temperature is less than 0.2% as seen from Eq. (15).

3. Drag coefficient

Figure 4a shows the experimentally determined values for the drag coefficient, γ_{ex}, measured in units of the theoretically expected drag coefficient, γ_{Stokes}, for 24 individual beads. The error-bars on the individual data-points are the propagated errors from the fit to Faxén's law and the uncertainty in the temperature, with a root-mean-square value of 0.5%. This high precision results from the long measurement time and the 50 determinations of γ for each bead. Any systematic error e.g. an undetected error in the specifications of the piezo-stage will offset the mean value of γ_{ex} but will not change the position of the data-points relative to each other. In other words, systematic errors directly influence the accuracy of the method, but do not influence the precision. We check the accuracy by comparing to γ_{Stokes} including its estimated errors. The shaded area shows the 2.3% error on γ_{Stokes} from the propagated uncertainty on the viscosity (temperature) and the bead radius.

The measured value for γ_{ex} in units of γ_{Stokes} was 1.005 ± 0.003 (mean $\pm$ SE, $n = 24$). As seen in Fig. 4a, the experimental value for an individual bead may deviate several percent from the theoretically expected value γ_{Stokes} even if the average value does not. Thus, if γ_{Stokes} is used for calibration, stochastic errors of several percent is expected due to the poly-dispersity of bead radii.

We were able to measure the poly-dispersity of the bead population because the precision of our calibration method (error-bar on single-bead datum) was smaller than this poly-dispersity. The standard deviation of the bead-population's various γ_{ex}-values was 1.5%, which is comparable to the 2% coefficient of variation for the bead diameter listed by the producer, and measured independently by us using TEM to 1.2%.

4. Trap stiffness

The experimentally determined trap stiffnesses are plotted in Fig. 4b. During the experiment the laser intensity and the temperature were kept constant and the trap stiffness was measured to be $(5.16 \pm 0.09) \times 10^{-2}$ pN/nm (mean $\pm$ SD, $n = 24$). The observed 1.7% variation from bead to bead is slightly larger than the variation in the drag-coefficient. It reflects, in addition to the poly-dispersity of the bead radii, stochastic variations in the

corner frequency and differences in material properties from bead to bead, e.g. in the density of polystyrene. However, since the trapping strength depends on the diameter of the bead, we expect κ_{ex} to correlate with γ_{ex}. A one-sided t-test gives a 99% probability ($t = 2.46$) that there is a positive linear correlation.
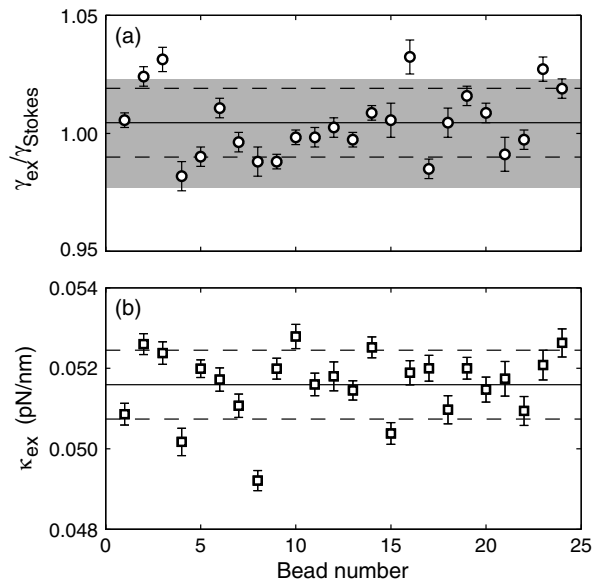

FIG. 4: Results from the calibration of 24 individual beads trapped close to a surface. Error-bars are the propagated errors from the fitting routines used, see text and [8] for details. Lines show the mean $\pm$ SD. (a): Measured drag coefficients Eq. (15), extrapolated to their bulk values according to Faxén's law, in units of the theoretically expected drag coefficient in bulk. The accuracy of the method is reflected by the agreement of the two values $\gamma_{ex}/\gamma_{Stokes} = 1.005 \pm 0.003$ (mean $\pm$ SE). The shaded region shows the estimated 2.3% uncertainty on γ_{Stokes}. (b): Measured trap stiffnesses Eq. (16). Additional variation compared to the drag coefficient is caused by variation in material properties of the individual bead as well as stochastic errors on the fit parameter f_c.

VI. DISCUSSION

Several popular calibration methods rely directly on an estimate for the drag coefficient. Since this parameter depends algebraically on the height of the bead above the surface, according to Faxén's law, a common approach is to perform the calibration far enough from the surface that only a correction of 5–10% has to be applied, given by the first term in Faxén's law. If the actual experiment is performed near the surface and an oil-immersion objective is used, this is an error-prone approach because the trap stiffness decreases rapidly with distance from the surface—10 μm from the surface, the stiffness is typically reduced by more than a factor of two for beads with a diameter of ~ 500 nm [8, 16, 17]. Thus, one detrimental effect is swapped for another, and calibration errors can

be large.

The calibration method presented here has some resemblance to a method used in [19]. There, a bead embedded in a gel was driven sinusoidally through the detection laser and the resulting spike in the PSD was used to estimate the sensitivity of the detection system. However, that method was not *in situ* since the bead used for the calibration could not be used for later experiments. The main strength of the calibration method presented here is that it is independent of estimates regarding the drag coefficient and that it can be performed on the location of the experiment.

This strength is also achieved in [6], which uses a calibrated acousto-optic deflector (AOD) to move the trap relative to the sample. This is done with a triangular-wave movement in short bursts lasting only 1% of the measurement time, to avoid losing the bead. It might be simpler, both experimentally and for the data analysis, to move the trap as we move our stage, and use power-spectrum analysis. *Continuous* movement of the trap requires ten times less amplitude to give unchanged signal power in Eq. (9) above for the same time of measurement. This reduces the risk of losing the trapped bead. Sinusoidal movement replaces [6, Fig. 4] with our spike ("scale-bar") in the power-spectrum, and any non-linearity stands out as spikes at integer multiples of f_{drive}. Also, the bead's co-movement with the trap is accounted for by the denominators in, e.g., our Eqs. (6) and (10), so it causes no calibration error. The second term in these denominators gives the relative importance of this co-movement.

Finally, the method of [6] requires the calibration of the AOD. For comparison, we get a known distance with one per mil accuracy from a factory-calibrated translation stage.

A. Experimental issues

We considered the following issues in the implementation of our calibration method using a stage.

1. Stage response:

Piezo stages have a finite response time, but this is not a problem here, since we drive with a sinusoidal signal. This is the signal form that another periodic signal degenerates to if the period is shorter than the response time. Also, any deviation from the chosen signal shows up in the experimental power spectrum as distinct, isolated higher modes at frequencies that are integer multiples of the driving frequency. So the quality of the stage response to the driving signal is under easy and strict experimental control, because a simple sinusoidal drive is used.

Mechanical resonances of the experimental setup can be exited. Our setups have resonance frequencies starting at approximately 400 Hz. The excitation of a resonance will give rise to additional power in the PSD at the resonance frequency, hence is under experimental control.

Mechanical crosstalk between axes occurs, as seen in Fig. 1. However, as the equations of motion are linear, this does not influence the calibration.

Finally, the stage position was measured as a voltage drop over built-in capacitors and converted to meters using the conversion factor $1 \, \mathrm{mV} = 10 \, \mathrm{nm}$ with a precision better than 0.1% according to the piezo-stage data sheet.

2. Photodiode response

Photodiodes may act as filters, but the effect is well understood and can be accounted for [3, 11, 20]. Depending on the type of diode used (quadrant or position sensitive), the linearity of the response to bead displacements may also vary. The region of linearity is easily found by moving a stuck bead through the laser focus. The photodiode must be aligned with the piezo-stage, but this is easily tested by looking at the PSD of the bead positions in response to driving the stage along one of its axes.

3. Crosstalk

Crosstalk between the axial (z) and the lateral (x and y) channels from a quadrant-photodiode may lead to underestimates of f_c of up to 10%. This crosstalk shows up as additional power in the x, y-channels for frequencies below the z-corner-frequency: The PSD for the x and y channels will gain a "shoulder" in their plateau region. A likely source of the crosstalk is differences in amplification of the signals from the diode's four quadrants. By repositioning the diode relative to the laser so that a small offset from the center position (i.e. zero volts in x and y) is introduced, the crosstalk can be eliminated [3, 8].

4. Laser heating of the liquid

The laser heats up the liquid locally, resulting in a decrease in viscosity. We looked for this effect by varying the laser intensity, but did not find any such effect when working close to surfaces. This result is to be expected because the glass cover-slip acts as a heat-sink [18].

5. Hydrodynamic response of the sample

The calibration method presented here relies on the liquid co-moving with the stage. In Appendix A we calculate the response of the liquid to the oscillatory movement of the stage. Close to the surface, the no-slip boundary condition entrains the liquid. Further

into the sample, the degree of entrainment depends on the height of the sample d and the drive frequency. If $d^2 \pi f_{\mathrm{drive}} < \nu \approx 1\,\mu\mathrm{m}^2/\mu\mathrm{s}$, where ν is the kinematic viscosity, the liquid co-moves in the entire flow-cell.

6. Shape of the trapped object

The only demand on the trapped object is that it does not rotate upon forced movement, in a manner that gives rise to a response in the detection system. This condition is fulfilled when the particle is either spherical, or asymmetric but strongly trapped. Due to the height dependence of the drag coefficient, even a spherical bead will rotate when translated close to a surface. But this rotation does not give rise to a signal from the photodiode because the bead is spherical and only displacements are detected. If the trapped object is elongated and weakly trapped, it may wobble in the trap in response to the oscillating liquid, and give rise to detection of false movement by the photodiode. Commercial micro-spheres are typically highly spherical, as are many small biological object, such as lipid droplets or micelles.

7. Shape of the trapping potential

Throughout this paper we assumed a parabolic trapping potential, but the method is not limited by this assumption. By choosing large drive amplitudes A, it is possible to map the shape of the potential and calibrate it. This is done by analyzing the higher modes of the bead's motion, that arise in response to a sinusoidal drive in a nonlinear trapping force-field.

VII. CONCLUSIONS AND OUTLOOK

A. Recommended approach

We suggest the following steps in experiments using a piezo-electric translation stage:

1. Trap the object of interest at the position of interest.

2. Drive the stage at $f_{\mathrm{drive}} = 16$ or $32\,\mathrm{Hz}$.

3. Collect position data from the photo detection system and the piezo-stage, with $f_{\mathrm{drive}}/\Delta f =$ an integer (to avoid leakage).

4. Determine A and f_{drive} from the PSD of the piezo-stage positions (or use previously calibrated values).

5. Determine D_{V} and f_{c} from a fit to the PSD of the bead-positions.

6. Determine the value of the spike in the PSD at f_{drive} and calculate β and κ_{ex} using Eqs. (13–16).

In point 2 the suggested values for f_{drive} are powers of two for ease of calculation of the appropriate t_{msr} and f_{sample}. They are also well below the resonance frequency of most systems, and low enough to ensure that the liquid co-moves with the stage, see Appendix A.

B. Imaging and non-imaging positional detection

Here we demonstrated our method, using positional detection in the non-imaging back-focal-plane of the condenser. Position detection in the image plane should also work, if the laser-trap remains stationary in the laboratory coordinate system, while the flow cell is driven.

Another approach moves the trapping laser relative to the flow-cell, e.g. using acousto-optic deflectors, galvano-mirrors, or some other beam-steering apparatus [1]. This approach works, if back-focal-plane detection is used: A pure translation of the laser in the image-plane produces no signal in the back-focal-plane, only a motion of the trapped object relative to the laser is detected. An advantage of this approach is that open samples can be used, because the sample is not moving. Furthermore, if the trap is driven with $f_{\mathrm{drive}}/f_{\mathrm{c}} > 10$ and the spike is two or more orders of magnitude above the thermal background Eq. (14) reduces to

$$\beta \simeq \frac{A}{\sqrt{2P_{\mathrm{V}}(f_{\mathrm{drive}})\Delta f}} \quad . \tag{18}$$

However, at high frequencies extra care has to be taken that the response of the photo-detection system is well characterized. Parasitic filtering and frequency-dependent hydrodynamics both remove power from the PSD at high frequencies—but only parasitic filtering affects β.

C. Atomic force microscopy

The method presented here should in principle also be applicable to the calibration of atomic force microscope (AFM) cantilevers in a liquid environment. The equations used to describe the motion of an AFM cantilever differ from our Eq. (2) by the inertial mass term, which cannot be neglected for a cantilever. In addition, the following problem must be surmounted before one can use our method for AFM: An expression for the frequency-dependent drag-coefficient of the cantilever must be known. Currently no useful analytical expressions exist, to the best of our knowledge.

D. *In situ* measurements

The method presented here can be implemented strictly *in situ.* Therefore, it should be applicable in situ-

ations that have so far eluded accurate measurements of positions and forces, e.g. when trapping spherical structures of unknown refractive index and size in the interior of cells. Or when measuring forces and viscosities inside micron-sized channels, i.e., the method described here could favorably be combined with microfluidic, lab-on-a-chip devices. Generally, position and force calibration should be possible in an arbitrary geometry because we do not need to know the corrections to the drag-coefficient due to the proximity of surfaces.

VIII. ACKNOWLEDGMENTS

APPENDIX A: HYDRODYNAMICS

Sometimes it is desirable to work with a flow-cell with open ends, e.g. to facilitate the exchange of buffer solution. When the ends are open, the liquid between the two cover-slips will generally not move with the same amplitude or phase as the flow-cell.

To calibrate we need to know the amplitude of the liquid's motion. We cannot measure this amplitude with an uncalibrated system, but we can calculate it. What we *can* measure is the phase of the liquid's motion, through the motion of the trapped bead, relative to the phase of the stage's motion. This measured phase-shift can then be compared to the phase-shift calculated below. Thus, the theory developed here is not used blindly. It is under experimental control.

We consider a liquid contained between two infinite, parallel planes, see Fig. 5. The planes are moved identically, parallel to themselves, in a simple sinusoidal fashion. In an experiment two sides of the flow-cell are sealed, increasing the drag force on the liquid: When oscillating a half-plan parallel to its edge there are additional friction forces because of the edge. In addition, the surface-tension at the openings will also force the liquid to move with the flow-cell. So, what we treat below is a worst-case scenario because it does not take these additional forces into account.

The velocity of the oscillating planes (the cover-slips) is zero in the y and z direction, and

$$v_{\text{drive}} = \omega A \cos(\omega t) \qquad (A1)$$

in the x-direction, where $\omega = 2\pi f_{\text{drive}}$. The only forces on the liquid are the shear forces arising from the no-slip

FIG. 5: Schematic drawing of the flow-cell seen from the side. The liquid is contained between the two glass cover-slips (shown in grey) at positions $z = 0$ and $z = d$.

boundary condition between the liquid and the accelerated planes. The liquid moves with the accelerated planes with a time-lag determined by the balance between the inertia of the liquid and the shear forces inside the liquid. Thus, we see that the velocity of the liquid can be written as $\vec{u}(x, y, z, t) = (u(z, t), 0, 0)$.

The equation of motion for the liquid is obtained from the linearized Navier-Stokes equations with constant pressure (see [21]):

$$\frac{\partial u}{\partial t}(z, t) = \nu \frac{\partial^2 u}{\partial z^2}(z, t) \ , \qquad (A2)$$

where ν is the kinematic viscosity of the liquid. The relevant solution to this equation can be written

$$u(z, t) = a(z)\cos(\omega t) + b(z)\sin(\omega t) \qquad (A3)$$
$$= A_{\text{liquid}}(z)\cos(\omega(t - t_{\text{phase}}(z))) \ , \quad (A4)$$

where $A_{\text{liquid}} = \sqrt{a^2 + b^2}$ and $\omega t_{\text{phase}} = \arctan(b/a)$. The coefficients a and b can be found by substituting Eq. (A3) into Eq. (A2):

$$a = -\frac{\nu}{\omega}b'' \quad \text{and} \quad b = \frac{\nu}{\omega}a'' \ , \qquad (A5)$$

from which we find

$$a'''' = -\left(\frac{\omega}{\nu}\right)^2 a \ , \qquad (A6)$$

where $'$ indicates differentiation with respect to z. The solution to Eq. (A6) is a linear combination of $\exp(\frac{\pm 1 \pm i}{\sqrt{2}}\sqrt{\frac{\omega}{\nu}}z)$ whose four coefficients are determined by the symmetry requirement $a(z) = a(d - z)$, and the boundary conditions $a(0) = \omega A$ and $a''(0) = 0$:

$$a(z) = c_1 \cos(\frac{z - d/2}{\zeta})\cosh(\frac{z - d/2}{\zeta})$$
$$+ c_2 \sin(\frac{z - d/2}{\zeta})\sinh(\frac{z - d/2}{\zeta}) \ , \quad (A7)$$

where

$$c_1 = \omega A \frac{\cos(\frac{d}{2\zeta})\cosh(\frac{d}{2\zeta})}{\cos^2(\frac{d}{2\zeta}) + \sinh^2(\frac{d}{2\zeta})} \qquad (A8)$$

$$c_2 = \omega A \frac{\sin(\frac{d}{2\zeta})\sinh(\frac{d}{2\zeta})}{\cos^2(\frac{d}{2\zeta}) + \sinh^2(\frac{d}{2\zeta})} \ , \qquad (A9)$$

and

$$\zeta = \sqrt{2\nu/\omega} \tag{A10}$$

is the depth of penetration of the shear-wave into the fluid. The expression for b follows from Eq. (A5) and is identical to Eq. (A7) except for c_1 and c_2 swapping places. When $d \gg \zeta$ the shear-wave's amplitude decreases exponentially as a function of z. When $d \ll \zeta$ the liquid co-moves with the planes as a solid body.

With the parameters used in the experiment far from surfaces, described in Sec. V, i.e., $f_{\text{drive}} = 28$ Hz, the penetration depth $\zeta = 107$ μm is larger than the thickness of the flow-cell $d \simeq 60$ μm. With these parameters, the amplitude of the liquid's motion differ at most 0.25% from the amplitude of the stage's motion, see Fig. 6. This result is independent of the amplitude A but is quite sensitive to d and f_{drive}. Thus, if working away from the surface it is important to choose f_{drive} so that it matches the thickness of the cell, i.e., so that $d/\zeta < 1$.
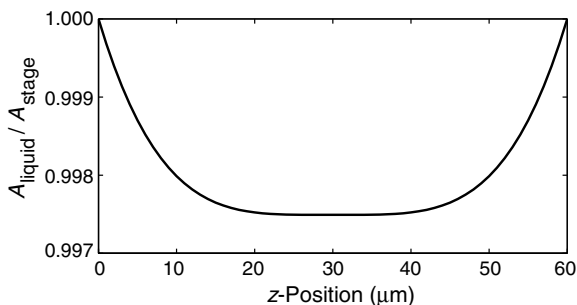

FIG. 6: Hydrodynamic prediction of the response of the liquid to the motion of the cover-slips. Abscissa: height above cover-slip z. Ordinate: Amplitude of liquid motion $A_{\text{liquid}}(z)$, Eq. (A4), in units of the amplitude of the oscillating planes $A_{\text{stage}} = A$. Parameters are the same as used in the experiment far from surfaces ($f_{\text{drive}} = 28$ Hz, $A = 208$ nm, $T = 23.0°$C).

It is illustrative to calculate the velocity of the liquid midway between the two planes, since this is where the motion of the liquid differ the most from that of the planes:

$$u(\frac{d}{2},t) = c_1 \cos(\omega t) + c_2 \sin(\omega t) \tag{A11}$$

$$= A_{\text{liquid}}(\frac{d}{2}) \cos(\omega(t - t_{\text{phase}}(d/2))) \tag{A12}$$

where now $A_{\text{liquid}}(\frac{d}{2}) = \sqrt{c_1^2 + c_2^2}$ and $\omega t_{\text{phase}}(d/2) = \arctan(c_2/c_1)$. When the cover-slips are close together or the drive frequency is very low $\frac{d}{2\zeta} \ll 1$, and we have $u(\frac{d}{2},t) = v_{\text{drive}}(t)$, i.e., the fluid co-moves with the planes. If the cover-slips are far apart or the drive-frequency is high Eq. (A12) becomes:

$$u(\frac{d}{2},t) = 2\omega A e^{-\frac{d}{2\zeta}} \cos(\omega t - d/2\zeta), \, d \gg 2\zeta \ , \tag{A13}$$

i.e., the amplitude decreases exponentially as d/ζ grows and the motion of the liquid is phase-shifted relative to the motion of the planes. These behaviors are illustrated in Fig. 7. From this we see the importance of choosing a drive-frequency small enough for the fluid to follow the flow-cell in the region where the trap is to be calibrated.
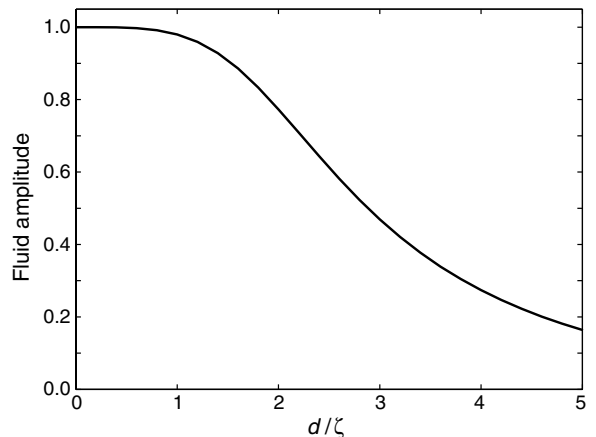

FIG. 7: Amplitude of liquid motion midway between cover-slips. Abscissa: The distance between two planes d, measured in units of the penetration depth ζ, Eq. (A10). Ordinate: Amplitude of the liquid-oscillations midway between the two planes $A_{\text{liquid}}(\frac{d}{2})$, Eq. (A12), measured in units of the amplitude of the oscillating planes. Notice the plateau at unity for small values of d/ζ where the fluid moves with the planes, and the exponential decay to zero at larger values where the liquid no longer follows the planes.

APPENDIX B: POWER SPECTRAL DENSITY FOR FINITE MEASUREMENT TIME

In Section III we calculated the PSD for the beads' motion, assuming infinite measurement time as well as continuous sampling. In an experiment, the data are collected for a finite time t_{msr} and with a finite sampling frequency f_{sample}. In what follows we are going to assume continuous sampling in time ($f_{\text{sample}} = \infty$ Hz). For the finite, but continuous, time Fourier transform of Eq. (5) we now have

$$\tilde{x}_k^{\text{rect}} = \int_{-t_{\text{msr}}/2}^{t_{\text{msr}}/2} dt \, e^{i2\pi f_k t} x(t) \ , \tag{B1}$$

and the expectation value for the one-sided ($f_k \geq 0$) PSD becomes:

$$P_k^{\text{rect}} = \frac{2\langle|\tilde{x}_k^{\text{rect}}|^2\rangle}{t_{\text{msr}}} = \frac{D + (f_{\text{drive}} r_k A)^2 t_{\text{msr}}}{\pi^2(f_k^2 + f_c^2)} \ , \tag{B2}$$

where

$$r_k = \frac{1}{\sqrt{2}} \frac{\sin(\pi(f_k - f_{\text{drive}})t_{\text{msr}})}{(f_k - f_{\text{drive}})t_{\text{msr}}} \ , \tag{B3}$$

gives the shape of the spike in the PSD. Here, $f_k = k/t_{\mathrm{msr}}$, $k = 0, 1, 2, \ldots, N/2$, and $N = t_{\mathrm{msr}} f_{\mathrm{sample}}$. In Eq. (B3) we have ignored cross terms of the type $\sin(\pi(f_k - f_{\mathrm{drive}})t_{\mathrm{msr}}) \sin(\pi(f_k + f_{\mathrm{drive}})t_{\mathrm{msr}})$, as they are typically several orders of magnitude smaller than the terms retained.

When the drive and sampling frequencies are chosen such that $f_{\mathrm{drive}} = f_k$, for some k, the spike consists of a single datum

$$r_k = \frac{\pi}{\sqrt{2}}\, \delta_{f_k, f_{\mathrm{drive}}} \tag{B4}$$

and the PSD becomes

$$P_k^{\mathrm{rect}} = \frac{D}{\pi^2(f_k^2 + f_c^2)} + \frac{\frac{1}{2} f_{\mathrm{drive}}^2 A^2}{f_k^2 + f_c^2} t_{\mathrm{msr}}\, \delta_{f_k, f_{\mathrm{drive}}} \tag{B5}$$

where $\delta_{f_k, f_{\mathrm{drive}}}$ is Kronecker's delta. This is the discrete version of the expression given in Eq. (9). We also see that the height of the spike depends linearly on the measurement time t_{msr}. When the measurement time is increased the spike approaches Dirac's delta function

$$t_{\mathrm{msr}}\, \delta_{f_k, f_{\mathrm{drive}}} \to \delta(f - f_{\mathrm{drive}}), \; t_{\mathrm{msr}} \to \infty \tag{B6}$$

and the expression in Eq. (9) is regained.

[1] K. C. Neuman and S. M. Block, Review of Scientific Instruments **75**, 2787 (2004).

[2] M. J. Lang, C. L. Asbury, J. W. Shaevitz, and S. M. Block, Biophysical Journal **83**, 491 (2002).

[3] K. Berg-Sørensen and H. Flyvbjerg, Review of Scientific Instruments **75**, 594 (2004).

[4] H. Faxén, Arkiv för Matematik, Astronomi och Fysik **17**, 1 (1923).

[5] S. B. Smith, Y. Cui, and C. Bustamante, Science **271**, 795 (1996).

[6] K. C. Vermeulen *et al.*, Review of Scientific Instruments **77**, 013704 (2006).

[7] M. Capitanio, R. Cicchi, and F. S. Pavone, Eur. Phys. J. B. **46**, 1 (2005).

[8] E. Schäffer, In preparation (2006).

[9] U. Bockelmann *et al.*, Biophysical Journal **82**, 1537 (2002).

[10] F. J. Harris, Proc. IEEE **66**, 51 (1978).

[11] K. Berg-Sørensen, L. Oddershede, E.-L. Florin, and H. Flyvbjerg, Journal of Applied Physics **93**, 3167 (2003).

[12] S. F. Tolić-Nørrelykke and H. Flyvbjerg, in preparation (2006).

[13] I. M. Tolić-Nørrelykke, K. Berg-Sørensen, and H. Flyvbjerg, Computer Physics Communications **159**, 225 (2004).

[14] P. M. Hansen, I. M. Tolić-Nørrelykke, H. Flyvbjerg, and K. Berg-Sørensen, Computer Physics Communications (to appear).

[15] S. Hell, G. Reiner, C. Cremer, and E. H. K. Stelzer, Journal of Microscopy-Oxford **169**, 391 (1993).

[16] E.-L. Florin, A. Pralle, E. H. K. Stelzer, and J. K. H. Hörber, Applied Physics A: Materials Science & Processing **66**, 75 (1998).

[17] K. C. Neuman, E. A. Abbondanzieri, and S. M. Block, Optics letters **30**, 1318 (2005).

[18] E. J. G. Peterman, F. Gittes, and C. F. Schmidt, Biophysical Journal **84**, 1308 (2003).

[19] K. Svoboda, C. F. Schmidt, B. J. Schnapp, and S. M. Block, Nature **365**, 721 (1993).

[20] K. Berg-Sorensen *et al.*, preprint (2006).

[21] L. D. Landau and E. M. Lifshitz, *Fluid Mechanics*, Vol. 6 of *Course of Theoretical Physics* (Pergamon Press, Oxford, 1959).